ADVANCED FUNCTIONAL MATERIALS

Supporting Information

for *Adv. Funct. Mater.,* DOI: 10.1002/adfm.202103171

Decoupling the Impacts of Engineering Defects and Band Gap Alignment Mechanism on the Catalytic Performance of Holey 2D CeO_{2-x}-Based Heterojunctions

Xiaoran Zheng, Sajjad S. Mofarah,* Claudio Cazorla, Rahman Daiyan, Ali Asghar Esmailpour, Jason Scott, Yin Yao, Sean Lim, Vienna Wong, Ewing Y. Chen, Hamidreza Arandiyan, Pramod Koshy,* and Charles C. Sorrell*

Supporting Information

Decoupling the Impacts of Engineering Defects and Bandgap Alignment Mechanism on the Catalytic Performance of Holey Two-Dimensional CeO_{2-x}-Based Heterojunctions

Xiaoran Zheng,[1] Sajjad S. Mofarah,[1] Claudio Cazorla,[1,2] Rahman Daiyan,[3] Ali Asghar Esmailpour Valmazouyi,[3] Jason Scott,[3] Yin Yao,[4] Sean Lim,[4] Vienna Wong,[1] Ewing Y. Chen,[1] Hamidreza Arandiyan,[5,6] Pramod Koshy,[1]* and Charles C. Sorrell[1]*

1 School of Materials Science and Engineering, UNSW Sydney, Sydney, NSW 2052, Australia
2 Now at Department of Physics, Polytechnic University of Catalonia, Campus Nord B4–B5, E–08034 Barcelona, Spain
3 Particles and Catalysis Research Group, School of Chemical Engineering, UNSW Sydney, NSW 2052, Australia
4 Electron Microscopy Unit (EMU), Mark Wainwright Analytical Centre, UNSW Sydney, Sydney, NSW 2052, Australia
5 Centre for Advanced Materials & Industrial Chemistry (CAMIC), School of Science, RMIT University, 124 La Trobe Street, Melbourne VIC 3000, Australia
6 Laboratory of Advanced Catalysis for Sustainability, School of Chemistry, University of Sydney, NSW 2006, Australia

[*] Corrseponding Authors:Xiaoran Zheng, Email: xiaoran.zheng@unsw.edu.au; Pramod Koshy, Email: koshy@unsw.edu.au

Experimental Section:

Chemicals and Materials: $Ce(NO_3)_6 \cdot 6H_2O$ (99.00%), $MoCl_3$ (99.95%), $RuCl_3$ (99.95%), and triethanolamine (TEA; ≥98.00%) were purchased from Sigma Aldrich (Sydney, Australia). Trichloroacetic acid (TCA; Cl_3CCOOH; ≥99.00%) was purchased from Chem–Supply Pty Ltd. (Sydney, Australia). The electrochemical three-electrode array consisted of a fluorine–doped tin oxide on glass (FTO; Wuhan Geao Scientific Education Instrument, Wuhan, China; film resistivity ~21 Ω square^{-1}) working electrode, a Pt plate (A = 4 cm^2) counter electrode, and Ag/AgCl reference electrode (Basi Inc., Evansville, IN, USA).

Synthesis of CeCP rod precursors: The synthesis was done using a chronopotentiometry technique incorporating an electrochemical station (Ezstat Pro, Crown Point, IN, USA; resolution 300 μV and 3 nA in the ±100 μA range) and the abovenamed electrodes. The initial electrolytes were prepared by adding TCA (0.05 M) and $Ce(NO_3)_3 \cdot 6H_2O$ (0.05 M) in a deionized (DI) water to make 150 mL of aqueous solution. The initial pH was 4.2, which subsequently was adjusted to 6.2 using concentrated NaOH (Sigma Aldrich, Sydney, Australia) solution (3 M). Prior to the synthesis of CeCP, the FTO substrates were sterilized progressively by ultrasonication in acetone, ethanol, and DI water (5 min for each). This was

followed by immersion in 40% nitric acid for 2 min to activate the surface, after which the same sterilization process was used, followed by drying with compressed air. The applied constant current was 30 mA for an FTO surface area of 15 cm^2 as this yielded high-quality film at rapid deposition rates.

Synthesis of CeCP and derived CeO_{2-x} morphologies: To synthesize the bulk CeO_2 nanotubes, CeCP (300 mg) precursor was dispersed in NaOH aqueous solution (2 M) and soaked for 30 min, followed by centrifuging at 5000 rpm for 10 min in polymer tubes. The same process was used five more times but with DI water for the purpose of cleaning. The resultant depolymerized CeCP was dried at 80°C in air for 24 h. The 2D–3D CeO_{2-x} nanostructure was fabricated by dispersing the depolymerized CeCP in TEA solution for 5 min using a magnetic stirrer at 300 rpm. The suspension then was transferred to an alumina crucible and calcined at 450°C for 4 h (heating rate 3°C/min). The resultant CeO_{2-x} nanosheet powders were stored in sealed containers prior to characterization and testing.

Synthesis of TMO hybrid nanostructures: The TMO–based hybrid nanostructures were synthesized using an identical procedure to that for CeO_{2-x} nanosheet powders except that the TM salts (4 mol%, metal basis) were added to the dispersion containing the CeCP when the TEA suspension was formed.

Characterization: Electron microscopy was done using dry CeO_{2-x} nanosheet powders that were suspended in water and drop–cast onto a carbon–coated Cu grid, followed by drying at room temperature. High-resolution transmission TEM (HRTEM) images and selected area electron diffraction (SAED) patterns of the nanostructures were done using a Philips CM200 field emission TEM (Eindhoven, the Netherlands). Scanning electron microscopy (SEM) images and energy dispersive X–ray spectroscopy (EDS) spectra were obtained using an FEI Nova Nano SEM (Hillsboro, OR, USA) in primary and secondary emission modes, with accelerating voltage in the range 10–15 kV.

X-ray photoelectron spectroscopy (XPS) was done using a Thermo Fisher Scientific ESCALAB 250Xi spectrometer (Loughborough, Leicestershire, UK) equipped with a monochromatic AlKα source (1486.6 eV) hemispherical analyzer. The chamber pressure during the analysis was held constant at < 0.8–1.0 kPa. The binding energies were referenced to the C 1s signal corrected to 285 eV and the spectra were fitted using a convolution of Lorentzian and Gaussian profiles. The data were normalized to eliminate the contributions from adventitious C (C 1s, 285 and 286 eV) and adsorbed H_2O (O 1s, 531 eV).

X–ray diffraction (XRD) patterns for the nanostructures were obtained using a Philips X'Pert Multipurpose X–ray diffractometer (Almelo, Netherlands) with CuKα radiation,

40 kV, 20 mA, scan range 20°–70° 2θ, step size 100.00 °2θ, scan speed 0.2 2θ/min). The peaks were analyzed using X'Pert High Score Plus software (Malvern, Gloucestershire, UK). Laser Raman microspectra were obtained using a Renishaw in Via confocal Raman microscope (Renishaw, Derbyshire, UK; helium–neon green laser, diffraction grating 1800 grooves/mm). All Raman data were recorded over the range 200–1500 cm^{-1} (resolution 1 cm^{-1}; laser power 35 mW; spot size ~2 μm diameter). The data analyses were performed using Renishaw WiRE 4.4 software and the spectra were calibrated against the silicon peak at ~520 cm^{-1}.

Photoluminescence (PL) spectroscopy was done using a Shimadzu Spectro Fluorophotometer RF–5301PC (Kyoto, Japan) at an excitation wavelength of 325 nm and room temperature. Electron Paramagnetic Resonance (EPR) analysis was conducted using a Bruker EMX X–Band ESR Spectrometer (Billerica, MA, USA), with constant frequency at 9.8 GHz. The EPR data were recorded over the center Field at 3200 mT, modulation amplitude at 4 G, and microwave power at 0.6325 mW. The processing on EPR spectra were carried out using Bruker Xenon software.

The thicknesses of the nanosheets were measured using a Bruker Dimension Icon SPM atomic force microscope (AFM; peak force tapping mode). The samples were deposited on glass substrates by extraction from the surface of a homogenous nanosheet/DI water suspension, deposition on a glass substrate, and drying in air. The AFM probe was a Bruker Nano Inc. ScanAsyst–Air Probe. The pixel resolution was 512 samples/line. The scan size was set to 2 μm × 2 μm, with a scan rate of 0.7 Hz. The peak force set point and the feedback gain settings were optimized accordingly. The AFM images were processed using Nanoscope Analysis 1.7 and the thicknesses of the holey 2D nanosheets were determined using the height profile from the processed images. Amplitude modulated Kelvin probe force microscopy (AM–KPFM) was performed using a Bruker Dimension ICON SPM with a Nano Scope V controller. A Bruker SCM–PIT–V2 platinum–iridium coated AFM tip was used to obtain the work function changes.

Specific surface areas (SSA) and pore size distributions were obtained using the N_2 physisorption technique at –196°C on a Micrometrics Tristar 3030 (Altanta, GA, USA). These data were determined using the Brunauer–Emmett–Teller (BET) and Barrett–Joyner–Halenda (BJH) methods, respectively. Prior to analysis, the samples were degassed under vacuum at 150°C for 3 h using a Micromeritics Smart VacPrep unit (Atlanta, GA, USA).

The UV–Vis reflectance data were collected using a PerkinElmer Lambda 1050 double–beam UV/Vis/NIR spectrophotometer (Waltham, MA, USA), with a triple detector for

maximal sensitivity. The wavelength range was 200–1500 nm. The optical indirect band bap was calculated using the Kubelka-Munk function.

Electrochemical Characterization: To prepare the electrodes, the catalyst (5 mg), MoO_3 (5 mg) (Sigma Aldrich, 99.99%), or RuO_2 (5 mg) (Sigma Aldrich, 99.99%) was suspended in deionized water (0.5 ml) and ethanol mixture (1:1, v/v), followed by the addition of Nafion solution (25 µL; Sigma Aldrich, 99.99%). The mixture was sonicated thoroughly to form a homogeneous ink. The working electrodes then were prepared by drop-casting the catalyst ink onto Teflon-treated carbon-fiber paper in order to achieve a total catalyst loading (0.5 mg cm^{-2}). The working electrode, graphite rod counter electrode, and saturated calomel reference electrode (SCE) were placed in a cell containing H_2SO_4 (1 M; 60 ml; pH = 0). All electrochemical measurements were done using a (CH Instruments, Inc. CHI 760E electrochemical workstation (Bee Cave, TX, USA). All potentials (E) measured were converted to the reversible hydrogen electrode (RHE) reference for the purpose of comparison, using the equation E_{RHE} (V) = E_{SCE} (V) + 0.245 + 0.059 × pH. Impedance electron spectroscopy (EIS) and cyclic voltammetry (CV) were carried out in Na_2SO_4 (0.5 M) solution at pH 6.8. EIS was measured under –0.4 V *vs* RHE with frequencies from 100 kHz to 0.1 Hz. Different scan rates were used in the cyclic voltametric measurement at the potential window of 0.6-0.65 V *vs* RHE in order to obtain the electrochemical capacitance current for evaluation of the relative electrochemically active surface area (ECSA).

Hydrogen thermal treatment is a simple and effective technique for generating defects like oxygen vacancy on the surface of the catalysts. Hence, as-prepared samples were reduced with hydrogen using a cylindrical electric furnace. In this procedure, samples were initially heated to 150°C under 30 mL min^{-1} pure nitrogen for 30 min to remove the surface moisture and impurities. Then, samples were cooled down to the ambient temperature and reheated to 500°C under N_2 atmosphere. After heating to 500°C, the gas was changed to 10% H_2 and 90% N_2 (99.99% Coregas, Australia) and the temperature was maintained at 500°C for 180 min.

Catalytic Ozonation Characterization: The catalytic ozonation reaction with salicylic acid (SA) as model contaminant was carried out in a semi batch reactor in which the aqueous phases including organic contaminant was in batch state and ozone gas was continuously bubbled into the solution from the bottom of the reactor. Experiments were performed under ambient conditions using simulated wastewater containing SA with the initial concentration (200 mg/L). In each trial, catalyst (10 mg/L) was added to the reactor and magnetically stirred for 60 min

at 750 rpm to reach the adsorption-desorption equilibrium. Ozone was introduced to the reactor with a flowrate (750 ml min^{-1}) using a BMT 802 N ozone generator (Messtechnik, Germany).

Samples were withdrawn from the reactor at selected times (0, 5, 10, 15, 30, 45 and 60 min) using a dispenser and filtered through a 0.45 μm. Then, ozone (0.025 mol) was added to these samples to quench the residual aqueous ozone and then analyzed. All experiments were repeated to determine the reproducibility of the results.

The aqueous ozone concentration was measured using the indigo colorimetric technique. The difference in light absorption between a blank (MilliQ water) and taken sample at wavelength of 600 nm is the basis of this technique. A Shimadzu 3000 UV-vis spectrophotometer was utilized to measure the light absorption. In addition, the total organic carbon (TOC) as an index of catalyst performance was determined using the Shimadzu TOC-VCH analyzer.

Spin-Polarized Density Functional Theory Characterization: Spin-polarized density functional theory (DFT) calculations were performed to characterize the electronic properties of the Mo-CeO_2 and Ru-CeO_2 interstitial solid solutions and MoO_3–CeO_2 and RuO_2–CeO_2 heterojunctions. The PBEsol functional was used as implemented in VASP software. A "Hubbard-*U*" scheme with $U = 3$ eV was employed for superior treatment of the localized Ce 4f and Mo and Ru 4d electron orbitals. The "projector augmented wave" method was used to represent the ionic cores by considering the following electrons as valence: Ce 4f, 5d, 6s, and 4d; Mo 4d and 5s; Ru 4d and 5s; and O 2s and 2p. Wave functions were represented in a plane-wave basis truncated at 650 eV.

For integrations within the first Brillouin zone, Monkhorst-Pack k-point grids were employed with a density equivalent to that of 16×16×16 for the fluorite CeO_2 unit cell. Periodic boundary conditions were applied along the three lattice vectors defining the simulation supercell; geometry relaxations were performed with a conjugate-gradient algorithm that optimized the ionic positions and the volume and shape of the simulation cell. The relaxations were halted when the forces in the atoms were < 0.01 eV·$Å^{-1}$. Using these parameters, the obtained energies were converged to within 0.5 meV per formula unit. The range-separated hybrid HSE06 exchange-correlation functional was used for accurate estimation of the electronic energy levels of the equilibrium geometries generated with the PBEsol+*U* functional. The value of the theoretical valence and conduction energy band edges referred to the Fermi energy level were determined through analysis of the projected densities of electronic states obtained in the spin-polarized DFT calculations.

For the MoO_3–CeO_2 and RuO_2–CeO_2 heterojunction calculations, ceria nanosheets were simulated as CeO_2 slabs of two-unit cells thickness oriented along the {111} direction (with chemical formula $Ce_{16}O_{32}$). A vacuum region of 25 Å was considered in all the slab simulations. Subsequently, a number of Mo and Ru ions compatible with the compositions for MoO_3 and RuO_2 and the crystal symmetries of MoO_3 (space group *Pnma*) and RuO_2 (space group $Fm\bar{3}m$) were adsorbed on both sides of the CeO_2 slabs. To describe the Mo–CeO_2 and Ru-CeO_2 interstitial solid solutions, a conventional CeO_2 fluorite unit cell containing 12 atoms (with chemical formula Ce_4O_8) was used.

The interstitial concentration in the DFT simulations calculations was fixed at 20 at% and the positions of the interstitial ions were identified with the high-symmetry central interstice in fluorite (½,½,½). The reduced species Mo^{5+} and Mo^{4+} were generated by introducing one and two oxygen vacancies (which intrinsically would be associated with Ce^{3+}), respectively, near the introduced transition metal ions.

Table S1. Comparison of physicochemical properties of functional nanosheets of different materials

Samples	Morphology	Thickness (nm)	Surface Area ($m^2 g^{-1}$)	Pore Volume ($cm^3 g^{-1}$)	Median Pore Size (nm)	Ref.
Mo-CeO_{2-x}	Holey nanosheet	1-3	147.73	0.33	6.04	Present work
CeO_{2-x}	Holey nanosheet	35	146.02	0.38	7.11	Present work
Ru-CeO_{2-x}	Holey nanosheet	5	270.54	0.76	7.60	Present work
Co_3O_4	Holey nanosheet	1.8	115	N/A	5.8	[1]
Co_3O_4	Nanosheet	2.1-5.8	N/A	N/A	N/A	[2]
$In_2O_3/ZnIn_2Se_4$	Nanosheet	2.8	N/A	N/A	N/A	[3]
MnO_{2-x}	Nanosheet	3	94	0.32	13.86	[4]
Co_3O_4/CeO_2	Nanosheet	3	N/A	N/A	N/A	[5]
PdO/CeO_2-Co_3O_4	Nanosheet	3.3	133.23	0.15	4.5	[6]
CdS-loaded 2D MOF	Nanosheet	7.1	44.7	0.24	21.7	[7]
$ZnMn_2O_4$	Holey nanosheet	~20ex	78.64	N/A	N/A	[8]
CeO_2	Nanosheet	20-50	68	N/A	N/A	[9]
$FeSe_2/g$-C_3N_4	Nanosheet	21.1	34	0.17	3.34	[10]

Table S2. Crystal radii and electronegativities of CeO_{2-x}, Mo-CeO_{2-x}, Ru-CeO_{2-x}

Samples	Element	Crystal Radius (nm)	Electronegativity (Pauling Units)	Oxide	Crystal Structure	Ref.
CeO_{2-x}	Ce(IV)	0.111	1.12	CeO_2	Cubic	[11]
Mo-CeO_{2-x}	Mo(IV)	0.079	2.16	MoO_2	Tetragonal	
	Mo(V)	0.060		Mo_4O_{11}	Orthorhombic	
	Mo(VI)	0.055		MoO_3	Orthorhombic	
Ru-CeO_{2-x}	Ru(IV)	0.076	2.20	RuO_2	Tetragonal	

Table S3. Possible heterojunction formation defect equilibria for Mo and Ru doping of CeO_{2-x}

Mo-Doping		
Region/Interface	**Process**	**Substitutional Solid Solubility**
Heterojunction	Ionic Charge Compensation	$5Mo_{Mo}^{x} + 15O_{O}^{x} \xrightarrow{CeO_2} 3Mo_{Ce}^{\cdot\cdot} + 2Mo_{Ce}^{\cdot} + 2V_{Ce}^{''''} + 7Ce_{S}^{x} + 15O_{O}^{x}$
	Electronic Charge Compensation	$2Mo_{Mo}^{x} + 6O_{O}^{x} \xrightarrow{CeO_2} Mo_{Ce}^{\cdot\cdot} + Mo_{Ce}^{\cdot} + 2Ce_{S}^{x} + 4O_{O}^{x} + O_2\ (g) + 3e'$
	Redox Charge Compensation	$2Mo_{Mo}^{x} + 6O_{O}^{x} \xrightarrow{CeO_2} Mo_{Ce}^{\cdot\cdot} + Mo_{Ce}^{\cdot} + 2Ce_{S}^{x} + 4O_{O}^{x} + O_2\ (g) + 3Ce_{Ce}'$
Region/Interface	**Process**	**Interstitial Solid Solubility**
Heterojunction	Ionic Charge Compensation	$3Mo_{Mo}^{x} + 9O_{O}^{x} \xrightarrow{CeO_2} Mo_{i}^{\cdot\cdot\cdot\cdot\cdot\cdot} + 2Mo_{i}^{\cdot\cdot\cdot\cdot\cdot} + 4V_{Ce}^{''''} + 4Ce_{S}^{x} + 9O_{O}^{x}$
	Electronic Charge Compensation	$2Mo_{Mo}^{x} + 6O_{O}^{x} \xrightarrow{CeO_2} Mo_{i}^{\cdot\cdot\cdot\cdot\cdot\cdot} + Mo_{i}^{\cdot\cdot\cdot\cdot\cdot} + 4O_{O}^{x} + O_2\ (g) + 11e'$
	Redox Charge Compensation	$2Mo_{Mo}^{x} + 6O_{O}^{x} \xrightarrow{CeO_2} Mo_{i}^{\cdot\cdot\cdot\cdot\cdot\cdot} + Mo_{i}^{\cdot\cdot\cdot\cdot\cdot} + 4O_{O}^{x} + O_2\ (g) + 11Ce_{Ce}'$
Ru-Doping		
Region/Interface	**Process**	**Substitutional Solid Solubility**
Heterojunction	Ionic Charge Compensation	$Ru_{Ru}^{x} + 2O_{O}^{x} \xrightarrow{CeO_2} Ru_{Ce}^{x} + Ce_{S}^{x} + 2O_{O}^{x}$
	Electronic Charge Compensation	$Ru_{Ru}^{x} + 2O_{O}^{x} \xrightarrow{CeO_2} Ru_{Ce}^{x} + Ce_{S}^{x} + 2O_{O}^{x}$
	Redox Charge Compensation	$Ru_{Ru}^{x} + 2O_{O}^{x} \xrightarrow{CeO_2} Ru_{Ce}^{x} + Ce_{S}^{x} + 2O_{O}^{x}$
Region/Interface	**Process**	**Interstitial Solid Solubility**
Heterojunction	Ionic Charge Compensation	$Ru_{Ru}^{x} + 2O_{O}^{x} \xrightarrow{CeO_2} Ru_{i}^{\cdot\cdot\cdot\cdot} + V_{Ce}^{''''} + Ce_{S}^{x} + 2O_{O}^{x}$
	Electronic Charge Compensation	$Ru_{Ru}^{x} + 2O_{O}^{x} \xrightarrow{CeO_2} Ru_{i}^{\cdot\cdot\cdot\cdot} + 2O_{O}^{x} + 4e'$
	Redox Charge Compensation	$Ru_{Ru}^{x} + 2O_{O}^{x} \xrightarrow{CeO_2} Ru_{i}^{\cdot\cdot\cdot\cdot} + 2O_{O}^{x} + 4Ce_{Ce}'$

Table S4. Interstitial solid solubility defect equilibria for Mo and Ru doping

Mo-Doping – Interstitial Solid Solubility		
Region/Interface	**Process**	**Defect Equilibria**
Heterojunction–to–Surface	IVCT	$Mo^{6+} + Ce^{3+} \rightarrow Mo^{5+} + Ce^{4+}$
Surface	Ionic Charge Compensation	$4Mo_{Mo}^{x} + 10O_{O}^{x} \xrightarrow{CeO_2} 4Mo_{i}^{\bullet\bullet\bullet\bullet\bullet} + 5V_{Ce}^{''''} + 5Ce_{S}^{x} + 10O_{O}^{x}$
	Electronic Charge Compensation	$2Mo_{Mo}^{x} + 5O_{O}^{x} \xrightarrow{CeO_2} 2Mo_{i}^{\bullet\bullet\bullet\bullet\bullet} + 4O_{O}^{x} + ½O_2\ (g) + 10e'$
	Redox Charge Compensation	$2Mo_{Mo}^{x} + 5O_{O}^{x} \xrightarrow{CeO_2} 2Mo_{i}^{\bullet\bullet\bullet\bullet\bullet} + 4O_{O}^{x} + ½O_2\ (g) + 10Ce_{Ce}'$
Surface–to–Subsurface	IVCT	$Mo^{5+} + Ce^{3+} \rightarrow Mo^{4+} + Ce^{4+}$
Subsurface	Ionic Charge Compensation	$Mo_{Mo}^{x} + 2O_{O}^{x} \xrightarrow{CeO_2} Mo_{i}^{\bullet\bullet\bullet\bullet} + V_{Ce}^{''''} + Ce_{S}^{x} + 2O_{O}^{x}$
	Electronic Charge Compensation	$Mo_{Mo}^{x} + 2O_{O}^{x} \xrightarrow{CeO_2} Mo_{i}^{\bullet\bullet\bullet\bullet} + 2O_{O}^{x} + 4e'$
	Redox Charge Compensation	$Mo_{Mo}^{x} + 2O_{O}^{x} \xrightarrow{CeO_2} Mo_{i}^{\bullet\bullet\bullet\bullet} + 2O_{O}^{x} + 4Ce_{Ce}'$
Ru-Doping – Interstitial Solid Solubility		
Region/Interface	**Process**	**Defect Equilibria**
Surface/Subsurface/Bulk	Ionic Charge Compensation	$Ru_{Ru}^{x} + 2O_{O}^{x} \xrightarrow{CeO_2} Ru_{i}^{\bullet\bullet\bullet\bullet} + V_{Ce}^{''''} + Ce_{S}^{x} + 2O_{O}^{x}$
	Electronic Charge Compensation	$Ru_{Ru}^{x} + 2O_{O}^{x} \xrightarrow{CeO_2} Ru_{i}^{\bullet\bullet\bullet\bullet} + 2O_{O}^{x} + 4e'$
	Redox Charge Compensation	$Ru_{Ru}^{x} + 2O_{O}^{x} \xrightarrow{CeO_2} Ru_{i}^{\bullet\bullet\bullet\bullet} + 2O_{O}^{x} + 4Ce_{Ce}'$

Table S5. Substitutional solid solubility defect equilibria for Mo and Ru doping of CeO_{2-x}

Mo-Doping – Substitutional Solid Solubility		
Region/Interface	**Process**	**Defect Equilibria**
Heterojunction–to–Surface	IVCT	$Mo^{6+} + Ce^{3+} \rightarrow Mo^{5+} + Ce^{4+}$
Surface	Ionic Charge Compensation	$4Mo_{Mo}^{x} + 10O_{O}^{x} \xrightarrow{CeO_2} 4Mo_{Ce}^{\bullet} + V_{Ce}'''' + 5Ce_{S}^{x} + 10O_{O}^{x}$
	Electronic Charge Compensation	$2Mo_{Mo}^{x} + 5O_{O}^{x} \xrightarrow{CeO_2} 2Mo_{Ce}^{\bullet} + 2Ce_{S}^{x} + 4O_{O}^{x} + ½O_2\ (g) + 2e'$
	Redox Charge Compensation	$2Mo_{Mo}^{x} + 5O_{O}^{x} \xrightarrow{CeO_2} 2Mo_{Ce}^{\bullet} + 2Ce_{S}^{x} + 4O_{O}^{x} + ½O_2\ (g) + 2Ce_{Ce}'$
Surface–to–Subsurface	IVCT	$Mo^{5+} + Ce^{3+} \rightarrow Mo^{4+} + Ce^{4+}$
Subsurface	Ionic Charge Compensation	$Mo_{Mo}^{x} + 2O_{O}^{x} \xrightarrow{CeO_2} Mo_{Ce}^{x} + 2O_{O}^{x}$
	Electronic Charge Compensation	$Mo_{Mo}^{x} + 2O_{O}^{x} \xrightarrow{CeO_2} Mo_{Ce}^{x} + 2O_{O}^{x}$
	Redox Charge Compensation	$Mo_{Mo}^{x} + 2O_{O}^{x} \xrightarrow{CeO_2} Mo_{Ce}^{x} + 2O_{O}^{x}$
Ru-Doping – Substitutional Solid Solubility		
Region/Interface	**Process**	**Defect Equilibria**
Surface/Subsurface/Bulk	Ionic Charge Compensation	$Ru_{Ru}^{x} + 2O_{O}^{x} \xrightarrow{CeO_2} Ru_{Ce}^{x} + 2O_{O}^{x}$
	Electronic Charge Compensation	$Ru_{Ru}^{x} + 2O_{O}^{x} \xrightarrow{CeO_2} Ru_{Ce}^{x} + 2O_{O}^{x}$
	Redox Charge Compensation	$Ru_{Ru}^{x} + 2O_{O}^{x} \xrightarrow{CeO_2} Ru_{Ce}^{x} + 2O_{O}^{x}$

Table S6. Comparison of CeO_2 XRD parameters for CeO_{2-x}, Mo-CeO_{2-x}, Ru-CeO_{2-x}

Sample	**{*hkl*}**	**2θ (°)**	**FWHM (*d*θ)**	**Crystallite Size (nm)**	**Average (nm)**
CeO_{2-x}	{111}	28.45701	0.97668	8.39139	8.13438
	{200}	32.98885	0.92237	8.98256	
	{220)	47.43510	1.06891	8.11777	
	{311}	56.31622	1.13832	7.91580	
Mo-CeO_{2-x}	{111}	28.80664	1.59368	5.14663	5.60770
	{200}	33.59743	1.50628	5.50921	
	{220)	48.01269	1.54590	5.62554	
	{311}	56.45820	1.46627	6.14941	
Ru-CeO_{2-x}	{111}	28.70051	1.68100	4.87813	5.06322
	{200}	33.23056	1.65840	4.99906	
	{220)	47.64309	1.72466	5.03525	
	{311}	56.62231	1.68968	5.34045	

Table S7. Assignment of Raman peaks for CeO_{2-x}, Mo-CeO_{2-x}, Ru-CeO_{2-x}

Samples	Raman Shift (cm^{-1})	Description	Reference
CeO_{2-x}	464	F_{2g} mode for CeO_2 (Ce–O_8 bond symmetric stretching)	[12]
	600	Defect-indexed (D) mode for CeO_2	[13]
Mo-CeO_{2-x}	790	O–Mo^{5+}–O bond vibrations in Mo_4O_{11}	[14]
	805	Mo^{6+}–O–X [X = Mo^{5+} or Ce^{4+}] bond vibrations	[15]
	823	A_g mode for MoO_3 (Mo^{6+}=O bond symmetric stretching)	[16]
	907	Mo^{5+}–O bond vibrations in Mo_4O_{11}	[14]
	950	Mo^{6+}=O bond vibrations (Mo in octahedral oxygen coordination, *i.e.*, heterojunction particle)	[17,18]
	995	A_g modes for MoO_3 (Mo^{6+}=O bond asymmetric stretching)	[16]
Ru-CeO_{2-x}	644	A_{1g} mode for RuO_2	[19]
	719	B_{2g} mode for RuO_2	[19]
	975	Ru–O–Ce bond vibrations	[20]

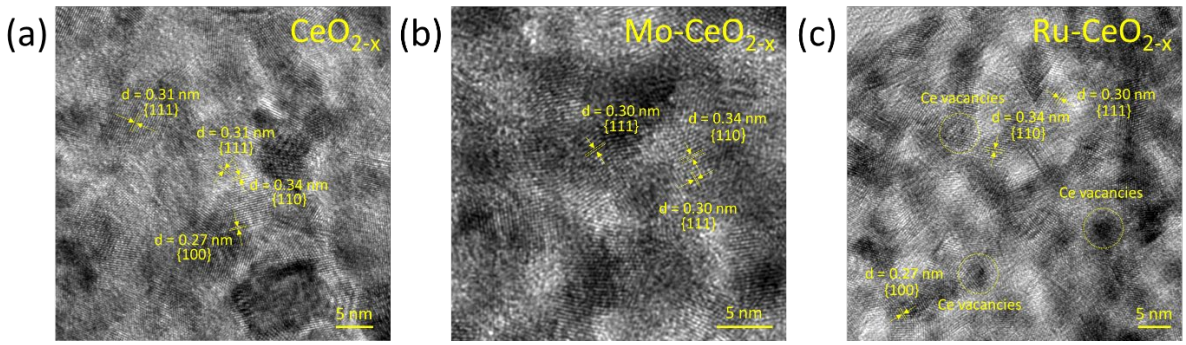

Figure S1. HRTEM images of holey nanosheets: **(a)** CeO_{2-x}, **(b)** Mo-CeO_{2-x}, **(c)** Ru-CeO_{2-x}

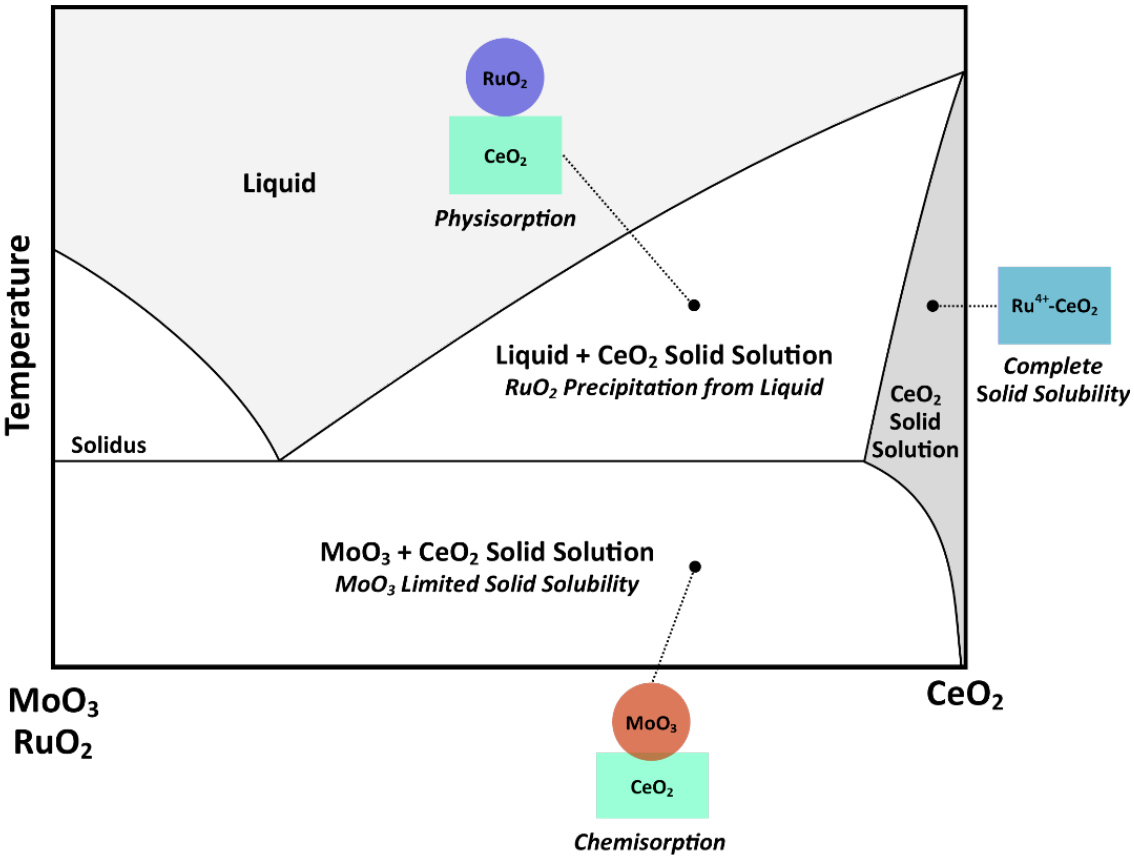

Figure S2. Representative phase diagram for doped CeO_{2-x}

Table S8. Nanostructural characteristics of CeO_{2-x}, Mo-CeO_{2-x}, Ru-CeO_{2-x}

Samples l	BET Surface Area ($m^2 g^{-1}$)	Pore Volume ($cm^3 g^{-1}$)	Median Pore Size (nm)
CeO_{2-x}	146.02	0.38	7.11
Mo-CeO_{2-x}	147.73	0.33	6.04
Ru-CeO_{2-x}	270.54	0.76	7.60

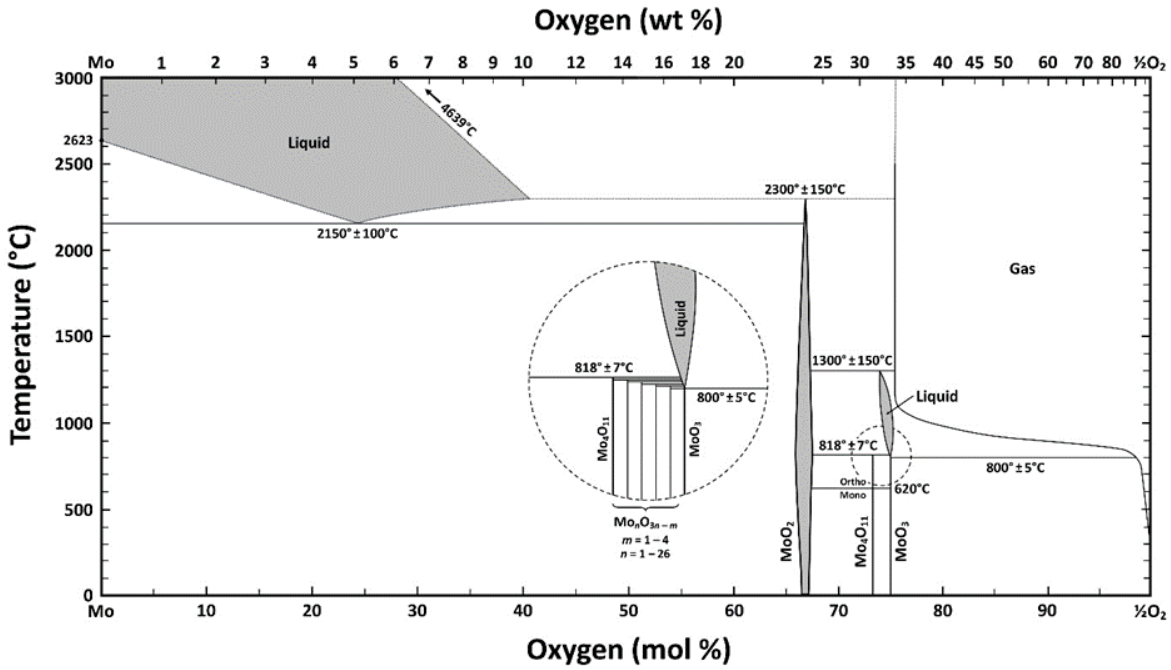

Figure S3. Mo-O phase diagram adapted from[21]

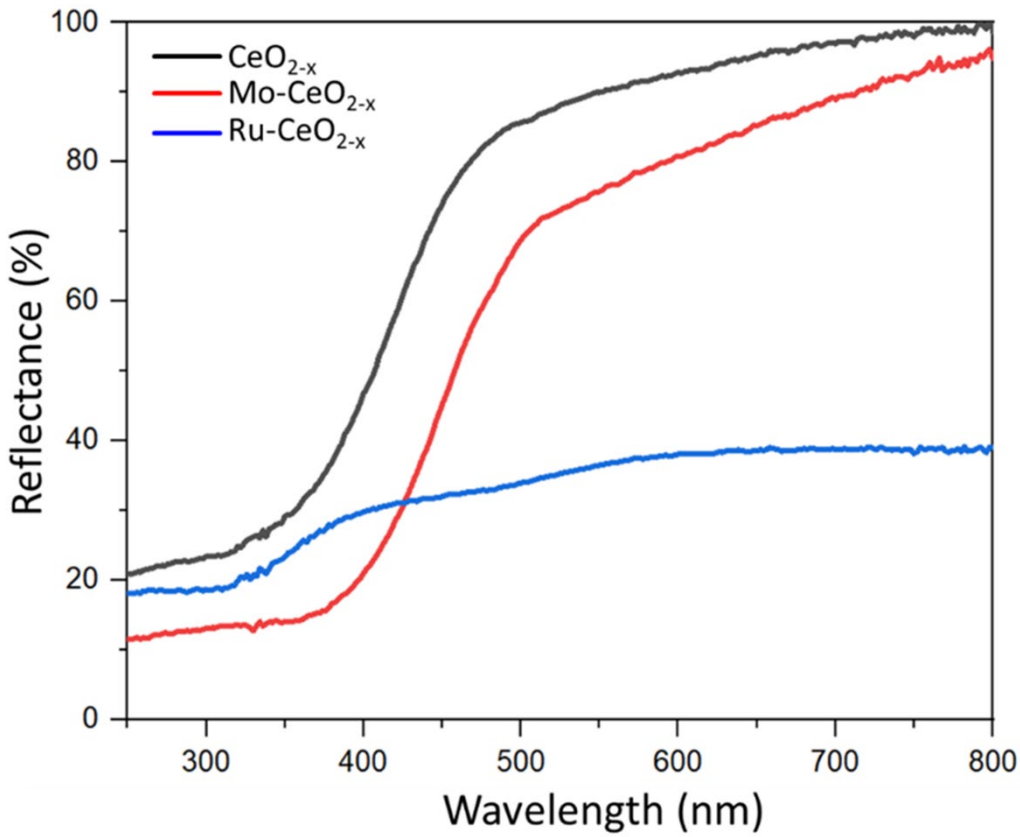

Figure S4. Reflectance UV-Vis spectrophotometry data for CeO_{2-x}, Mo-CeO_{2-x}, Ru-CeO_{2-x}

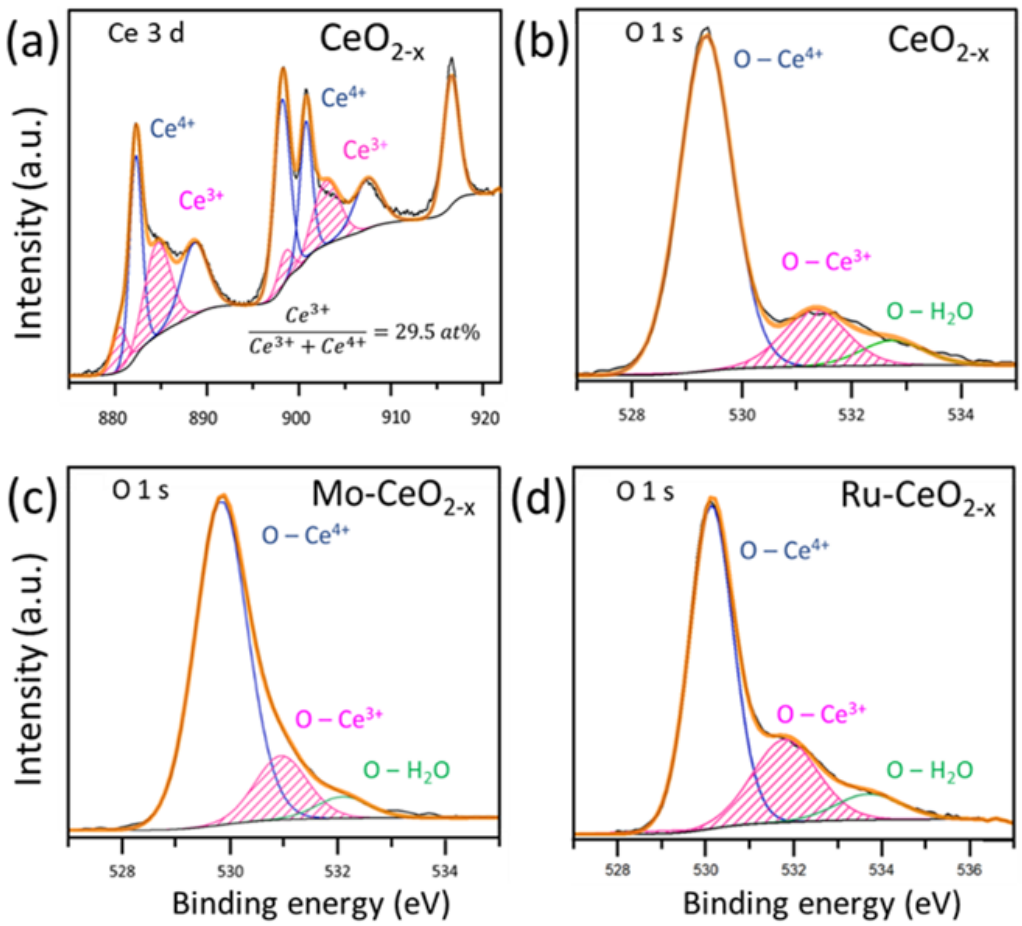

Figure S5. XPS spectra for CeO_{2-x}: **(a)** Ce 3 d, **(b)** O 1 s; XPS spectra for TMOs: **(c)** O 1 s for Mo, **(d)** O 1 s for Ru

As shown in **Figure S5**, the Ce $3d_{5/2}$ spectrum of pure CeO_{2-x} exhibits peaks at binding energies ~880 and ~885 eV, which are characteristic of Ce^{3+} (magenta), and peaks at ~882, ~889, and ~898 eV, which are characteristic of Ce^{4+} (blue). In principle, for pure CeO_{2-x} and *ionic charge compensation*, the concentration of oxygen vacancies ($[V_O^{\bullet\bullet}]$) is twice the concentration of Ce^{3+} ($[Ce^{3+}]$), the latter of which is determined from the normalized integrated areas for the Ce^{3+} peaks. However, in the case of CeO_{2-x} doped with cations of variable valence (stoichiometric or fractional), *redox charge compensation* through intervalence charge transfer (IVCT) can contribute to the formation or annihilation of $V_O^{\bullet\bullet}$. Further, *electronic charge compensation* does not affect the $[V_O^{\bullet\bullet}]$. The $[Ce^{3+}]$ concertation were calculated to be 29.5 at%, 28.7 at%, and 29.6 at% for CeO_{2-x}, Mo–CeO_{2-x}, and Ru–CeO_{2-x}, respectively, giving respective $[V_O^{\bullet\bullet}]$ of 14.8%, 14.4%, and 14.8%.

Table S9. Interpretation of XPS data summarized in **Table S9**.

Row	Parameter (at%)	Interpretation
1	**[Ce]**	Small decrease for Mo–CeO_{2-x} and larger decrease for Ru–CeO_{2-x} consistent with minor surface Mo solubility and major bulk Ru solubility, with ionic charge compensation by V_{Ce}''''
2	$[V_{Ce}'''']_{Theoretical}$	As in Row 1
3	**[O]**	Similar values for all three are consistent with effective absence of $V_O^{\bullet\bullet}$ formation and hence absence of associated acceptor Mo^{3+} or Ru^{3+}; simultaneous decrease in [Ce] is consistent with formation of V_{Ce}''''
4	**[Ce]/[O] Ratio**	As in Rows 1-3
5	**[O]/[Ce] Ratio**	As in Rows 1-3
6	**[O]/([Ce] + [X]) Ratio**	As in Rows 1-3
7	**[Ce]/([Ce] + [O])**	As in Rows 1-3
8	$[Ce^{3+}]/([Ce^{3+}] + [Ce^{4+}])$	Similar values for all three consistent with unchanged $[Ce^{3+}]$ as well as effectively unchanged surface $[Ce^{4+}]$ owing to exsolution from near-surface and deposition on surface; also consistent with absence of $V_O^{\bullet\bullet}$ formation, IVCT involving Ce, and redox charge compensation involving Ce
9	$[O–Ce^{3+}]/[O–Ce^{4+}]$	Similar CeO_{2-x} and Mo–CeO_{2-x} relative to large increase in Ru–CeO_{2-x} consistent with large bulk Ru solubility, redox charge compensation by Ce_{Ce}', ionic charge compensation by V_{Ce}'''', and loss of associated O–Ce^{4+}
10	$[O–Ce^{3+}]/([O–Ce^{3+}] + [O–Ce^{4+}])$	As in Row 9
11	$[V_O^{\bullet\bullet}]_{Hypothetical}$	As in Rows 1-3
12	$[V_O^{\bullet\bullet}]_{Hypothetical}$	As in Row 9
13	**[Dopant]**	As in Rows 1-3

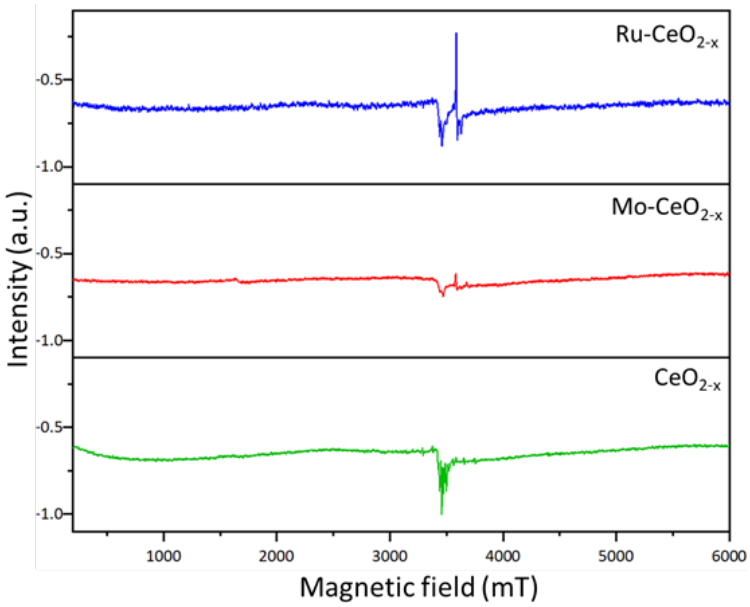

Figure S6. EPR spectra (equal sample masses) for CeO_{2-x}, Mo-CeO_{2-x}, Ru-CeO_{2-x}

Table S10. Description of observed EPR data for CeO_{2-x}, Mo-CeO_{2-x}, Ru-CeO_{2-x}

Sample	Magnetic Field (G)	g Factor	Description		Ref.
			Present Work	Literature	
CeO_{2-x}	3752	1.880	Ce^{4+}–Ce^{3+} redox (subsurface)	Ce^{3+}	[22]
	3656	1.930			
	3589	1.967	Ce^{4+}–Ce^{3+} redox (bulk)	Ce^{4+}–Ce^{3+}	[23,24]
	3522	2.006	$^{\bullet}O_2^{-}$–Ce^{4+} (oxygen vacancy cluster)	$^{\bullet}O_2^{-}$–Ce^{4+} (oxygen vacancy cluster)	[25-28]
	3499	2.011	$^{\bullet}O_2^{-}$–Ce^{4+} (isolated oxygen vacancy)	$^{\bullet}O_2^{-}$–Ce^{4+} (isolated oxygen vacancy)	[25-29]
	3473	2.029			
	3457	2.036			
	3438	2.048	$^{\bullet}O_2^{-}$–Ce^{4+} (oxygen vacancy cluster)	$^{\bullet}O_2^{-}$–Ce^{4+} (oxygen vacancy cluster)	[25-29]
	3427	2.050			
	3379	2.080	O_2–Ce^{3+} (adsorbed)	Ce^{3+}	[22,30]
	3291	2.140			
Mo-CeO_{2-x}	3679	1.914	Mo^{5+}	Mo^{5+}	[31]
	3630	1.940	Mo^{4+}–Ce^{3+} (bulk[a)])	X–Ce^{3+}	[24,32,33]
	3589	1.967	Mo^{4+}–Ce^{3+} (bulk)	X–Ce^{3+}	[24,32,33]
	3471	2.029	$^{\bullet}O_2^{-}$–Ce^{4+} (isolated oxygen vacancy)	$^{\bullet}O_2^{-}$–Ce^{4+} (isolated oxygen vacancy)	[25-29]
	3440	2.045	$^{\bullet}O_2^{-}$–Ce^{4+} (oxygen vacancy cluster)	$^{\bullet}O_2^{-}$–Ce^{4+} (oxygen vacancy cluster)	[25-29]]
Ru-CeO_{2-x}	3630	1.940	Ru^{4+}–Ce^{3+} (bulk)	X–Ce^{3+}	[24,32,33]
	3589	1.967	Ru^{4+}–Ce^{3+} (bulk)	X–Ce^{3+}	[24,32,33]
	3460	2.037	$^{\bullet}O_2^{-}$–Ce^{4+} (isolated oxygen vacancy)	$^{\bullet}O_2^{-}$–Ce^{4+} (isolated oxygen vacancy)	[25-29]
	3439	2.048	$^{\bullet}O_2^{-}$–Ce^{4+} (oxygen vacancy cluster)	$^{\bullet}O_2^{-}$–Ce^{4+} (oxygen vacancy cluster)	[25-29]

a) In the present work, the failure of Raman, a bulk analytical technique, to detect Mo^{4+} indicates that this valence is limited to the subsurface although the EPR signal is assigned to a bulk effect; that is, subsurface and bulk can be considered to be equivalent in EPR. However, it is possible that the Mo^{4+} diffusion extends somewhat into the bulk but at a concentration below the level of detection by Raman.

Table S11. Summary of photoluminescence data attributed to F center and related transitions in CeO_{2-x}

Wavelength (nm)	Energy (eV)	Assigned Transition	Ref.
310	4.00	F^{++} to O 2*p* (VB)	[34,35]
376	3.3	Ce $4f_1$ to CB	
384	3.23	Ce $4f_0$ to Ce $4f_1$	
404	3.07	F^{++} to CB	
428-413	2.9-3.0	Ce $4f_1$ to F^{++}	
517-496	2.4-2.5	F^{+} to CB F^{+} to Ce $4f_0$	
620-590	2.0-2.1	F^{0} to CB	
729	1.7	VB to F^{+}	

Table S12. Comparison between photoluminescence data attributions of Aškrabić *et al.*[34] and speculations of present work

Aškrabić *et al.*[34]			Present Work		
Wavelength (nm)	Energy (eV)	Assigned Transition	Wavelength (nm)	Energy (eV)	Alternative Interpretation
376	3.3	Ce $4f_1$ to CB	3.1	405	$V_O^{\bullet}$ (F^{+}) → V_O^{x} (F^{++})
428-413	2.9-3.0	Ce $4f_1$ to F^{++}	2.7	455	$V_O^{\bullet\bullet}$ (F^{0}) → $V_O^{\bullet}$ (F^{+})
517-496	2.4-2.5	F^{+} to F^{+}	2.3	540	Ce^{4+} → Ce^{3+} → $V_O^{\bullet}$ (F^{+})
620-590	2.0-2.1	F^{0} to F^{0}	2.1	590	$2Ce^{4+}$ → $2Ce^{3+}$ → $V_O^{\bullet\bullet}$ (F^{0})
729	1.7	VB to F^{+}	--	--	Ce^{4+} → Ce^{3+}

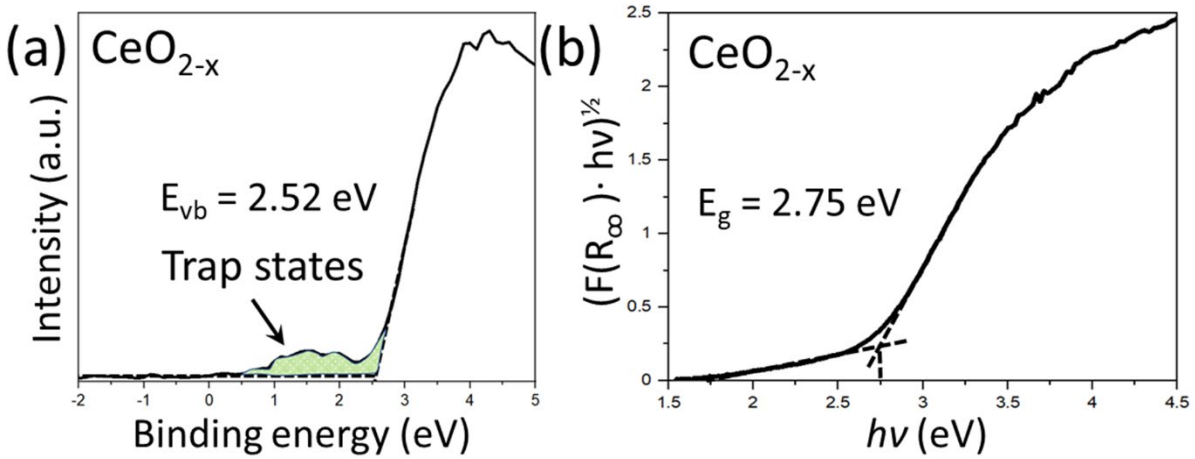

Figure S7. Band energy data for CeO_{2-x} holey nanosheets: **(a)** XPS valence band plot, **(b)** Kubelka-Munk plot from UV-Vis spectrophotometry for optical indirect band gap

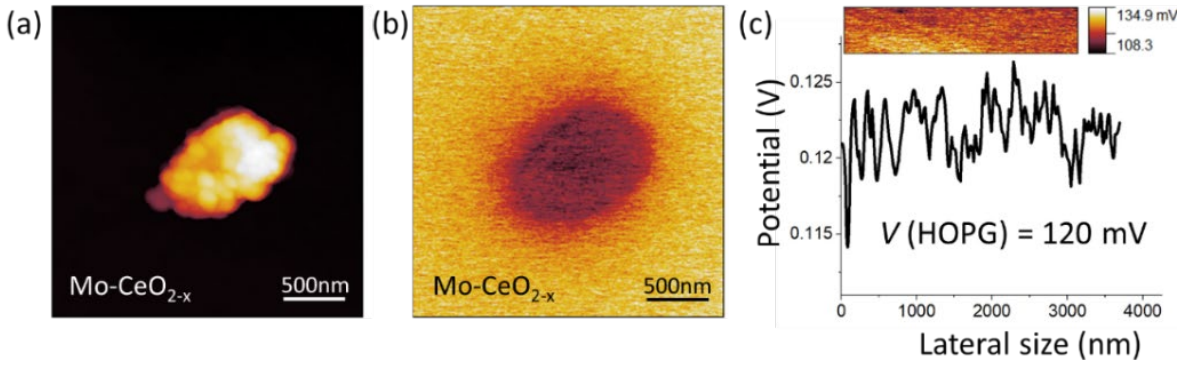

Figure S8. KPFM images of Mo-CeO_{2-x} holey nanosheet: **(a)** Topography, **(b)** Contact potential difference; Calibration data: **(c)** Image of contact potential difference and plot for highly oriented pyrolytic graphite (HOPG)

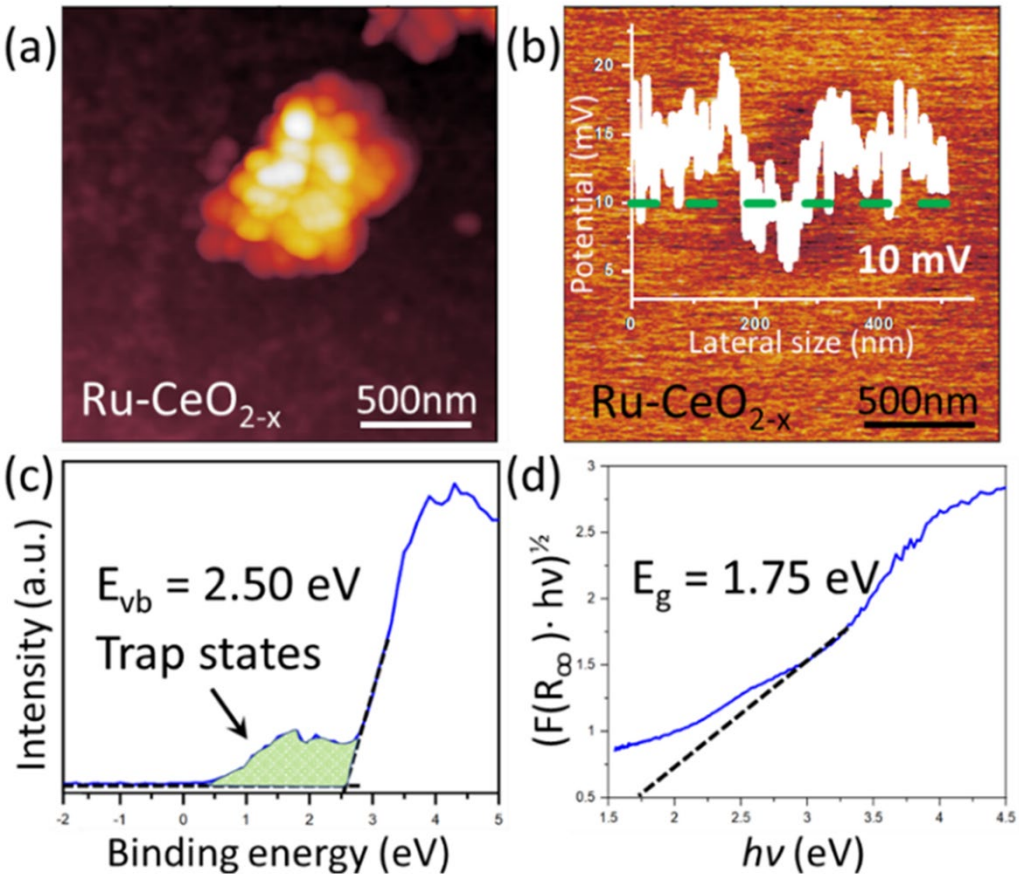

Figure S9. Band energy data for Ru-CeO_{2-x} holey nanosheets: **(a)** KPFM image of sample topography, **(b)** KPFM image of contact potential difference, **(c)** XPS valence band plot, **(d)** Kubelka-Munk plot from UV-Vis spectrophotometry for optical indirect band gap

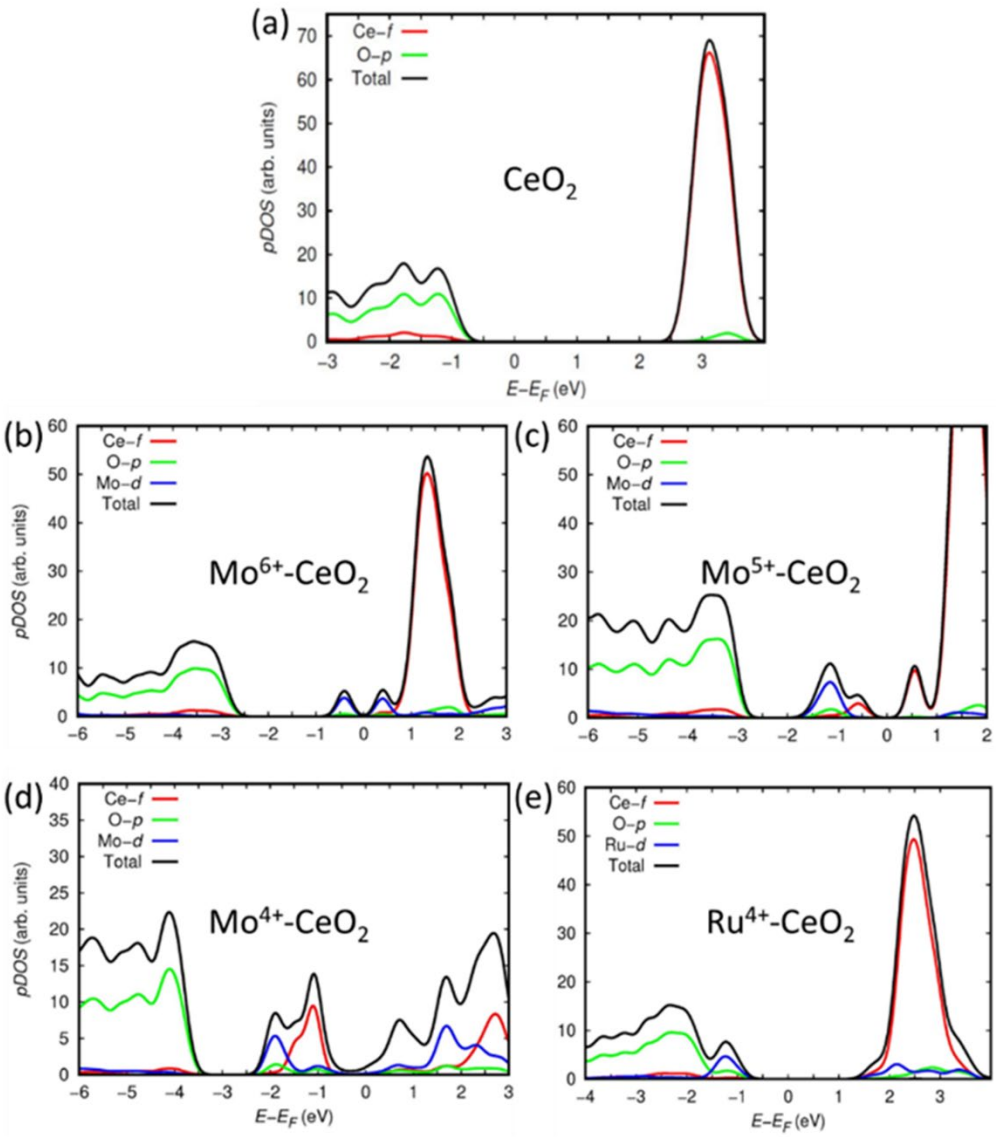

Figure S10. First-principles DFT simulations of electronic densities of states and band gaps for: **(a)** CeO_2, substitutional solid solubility: **(b)** Mo^{6+}-CeO_2, **(c)** Mo^{5+}-CeO_2, **(d)** Mo^{4+}-CeO_2, **(e)** Ru^{4+}–CeO_2

Table S13. Optical indirect band gaps from UV-Vis data and calculated by DFT

Condition		Optical Indirect Band Gap (eV)		
		CeO_{2-x}	Mo-CeO_{2-x}	Ru-CeO_{2-x}
Experimental		2.75	2.62	1.75
DFT	Interstitial Solid Solubility	3.20	Mo^{6+} 2.50	Ru^{4+} 1.75
			Mo^{5+} 1.75	
			Mo^{4+} 1.00	
	Substitutional Solid Solubility		Mo^{6+} 2.20	Ru^{4+} 2.50
			Mo^{5+} 1.75	
			Mo^{4+} 1.50	
	Heterojunction	--	MoO_3 3.30	RuO_2 3.10

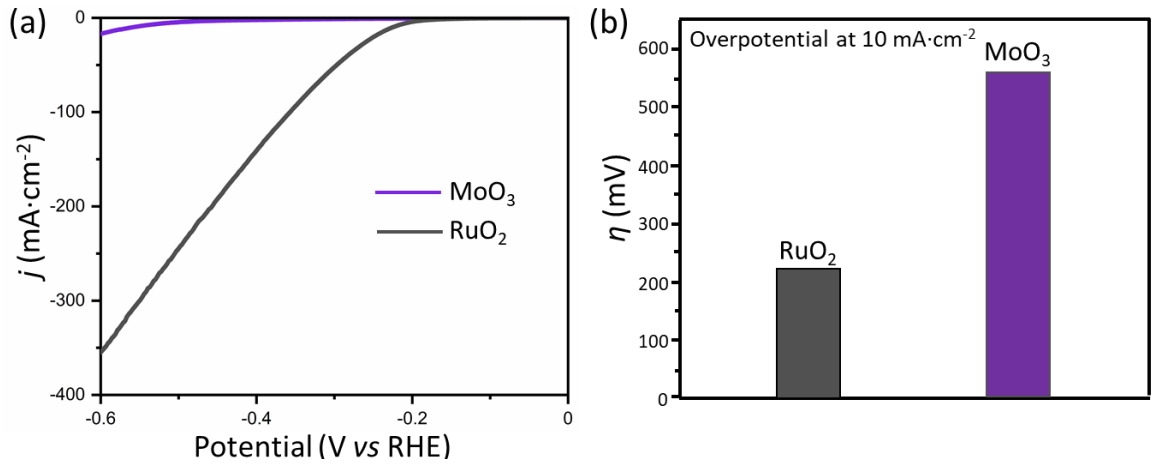

Figure S11. Electrocatalytic hydrogen evolution reaction (HER) performance of MoO_3 and RuO_2: (a) Linear sweep voltammetry curves (pH = 0) at scan rate of 5 mV s^{-1}, (b) Plot of the overpotential required to reach 10 mA cm^{-2}

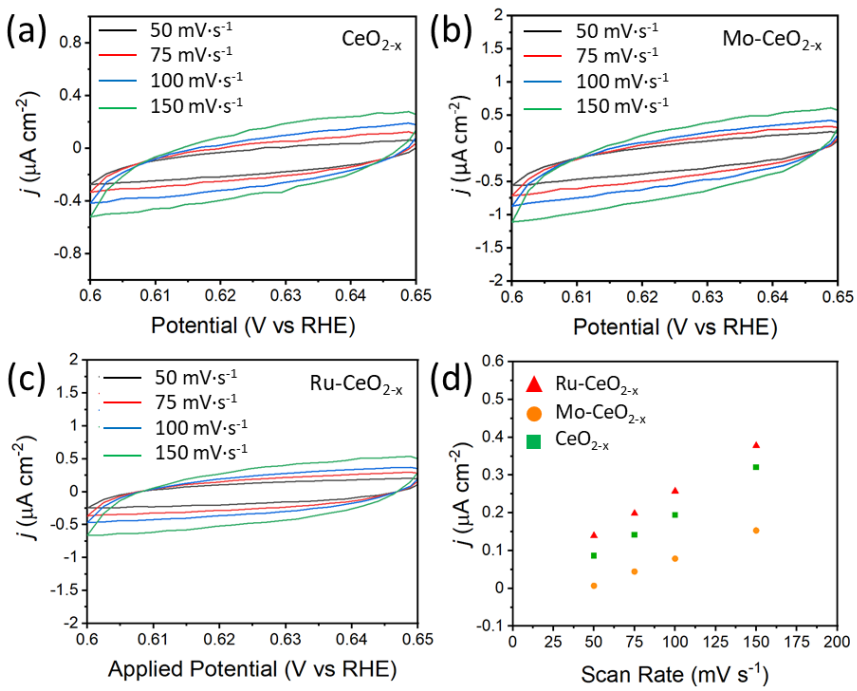

Figure S12. Electrochemical surface area (ECSA) measurements for CeO_{2-x}, Mo-CeO_{2-x}, Ru-CeO_{2-x} from cyclic voltammetry (CV) profiles for: **(a)** CeO_{2-x}, **(b)** Mo-CeO_{2-x}, **(c)** Ru-CeO_{2-x} in 1 M Na_2SO_4, **(d)** Dependence of capacitive current on scan rates at applied potential of 0.625 V *vs* RHE

The similarities of the three slopes in **Figure S12d** indicate that the ECSAs for the three catalysts are similar: CeO_{2-x} = 0.0022 $(\mu A \cdot s)(mV \cdot cm^2)^{-1}$, Mo-$CeO_{2-x}$ = 0.0015 $(\mu A \cdot s)(mV \cdot cm^2)^{-1}$, Ru-$CeO_{2-x}$ = 0.0024 $(\mu A \cdot s)(mV \cdot cm^2)^{-1}$

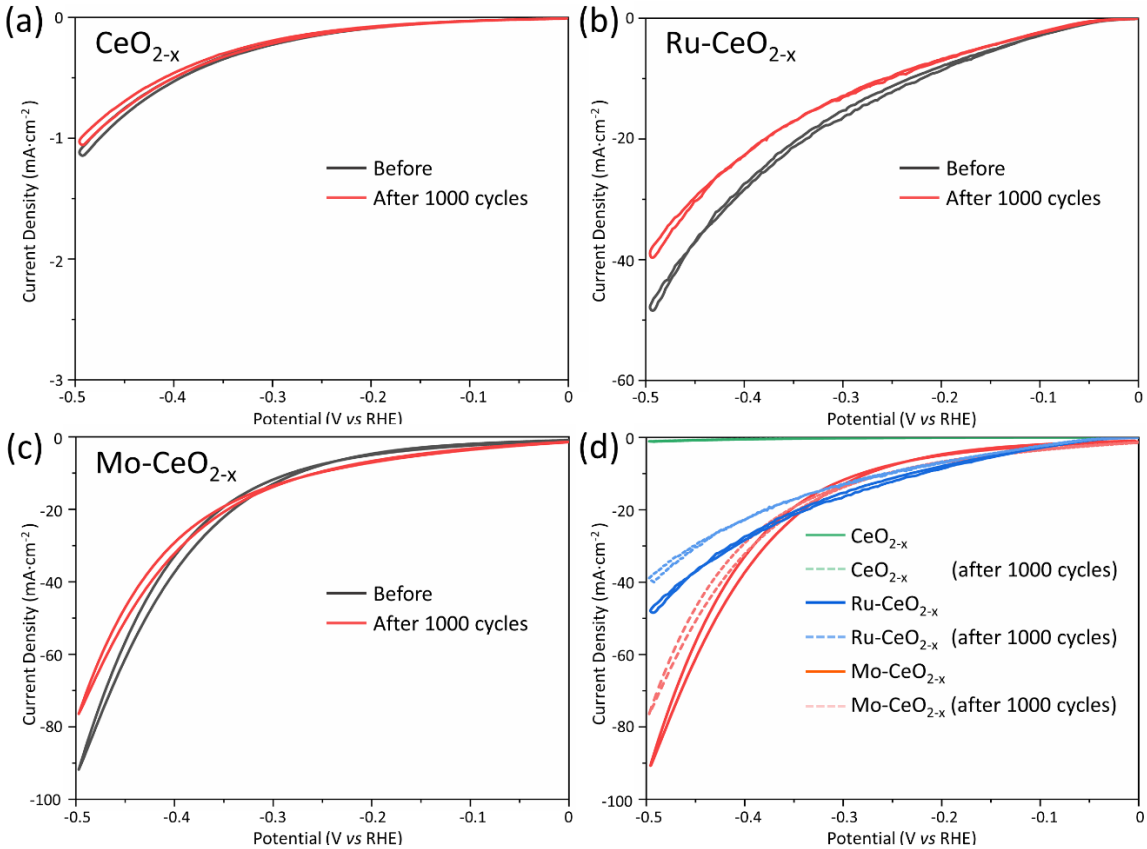

Figure S13. HER stability testing: (a) CeO_{2-x}; (b) Ru-CeO_{2-x}; (c) Mo-CeO_{2-x}; (d) Composite data

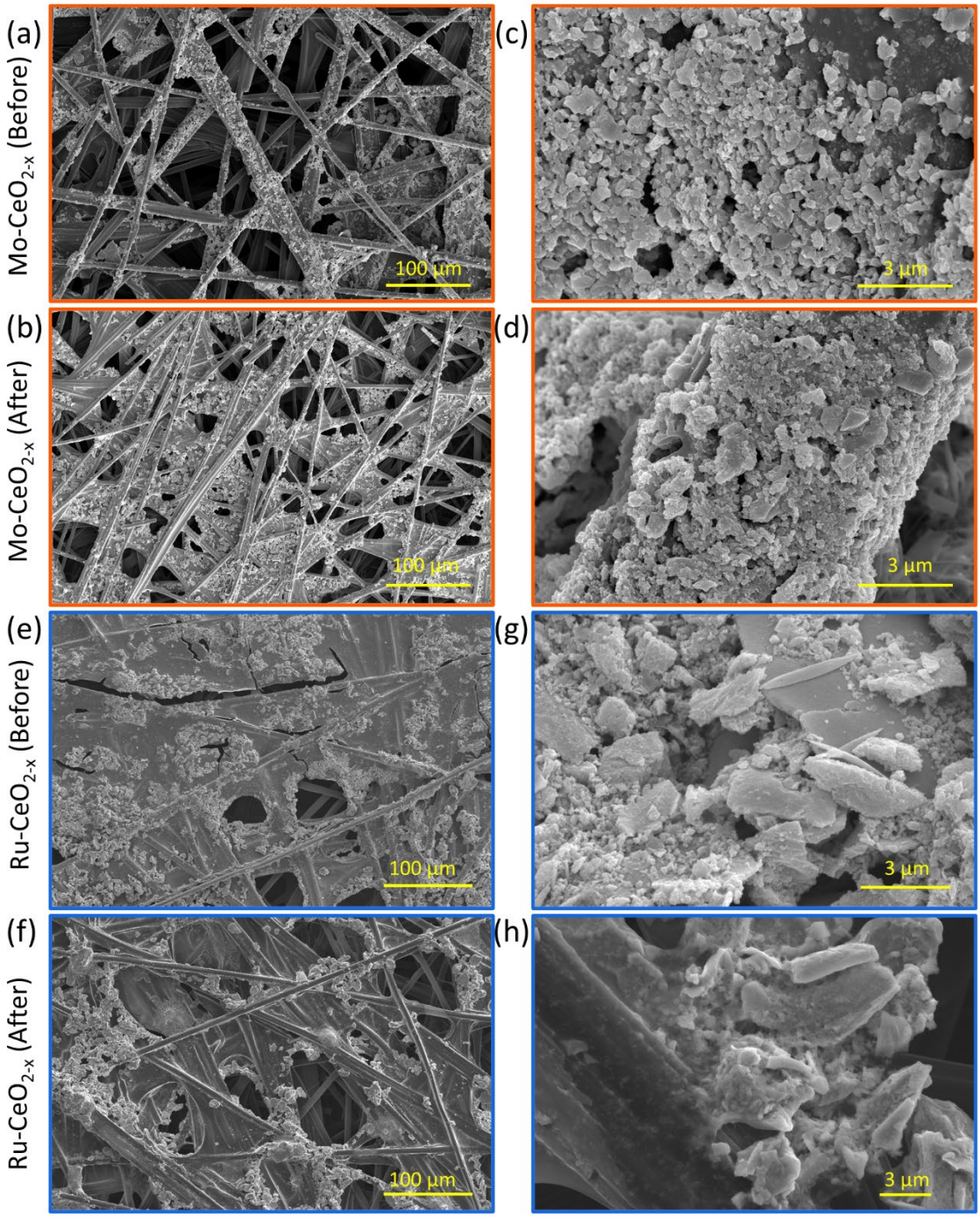

Figure S14. SEM images before and after HER stability testing: Mo-CeO_{2-x} – (a, c) before; (b, d) after; Ru-CeO_{2-x} – (e, g) before; (f, h) after

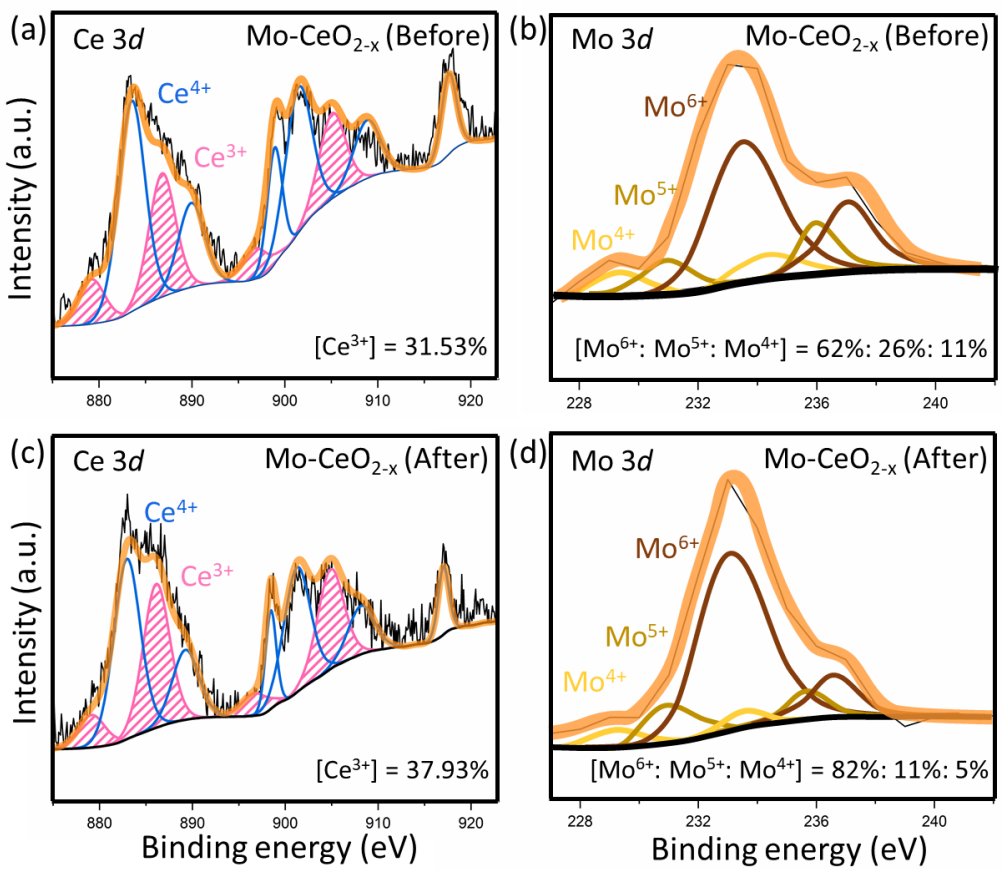

Figure S15. XPS analyses before and after HER testing of Mo-CeO_{2-x}: Before – (a) Ce 3*d*; (b) Mo 3*d*; after – (c) Ce 3*d*; (d) Mo 3*d*

Table S14. Comparison of overpotentials and corresponding Tafel slopes of CeO_{2x}-based samples

Sample	Solution	Overpotential (mV)	Tafel Slope (mV dec^{-1})	Reference
Mo (4 wt%)-CeO_{2-x}	Acidic	315	138	Present work
Ru (4 wt%)-CeO_{2-x}	Acidic	375	241	Present work
CeO_{2-x}	Acidic	590	357	Present work
Ni alloy matrix doping CeO_2	Basic	~1050	141	[36]
Ni–S alloy matrix doping CeO_2	Basic	N/A	157	[37]
NiO/CeO_2	Basic	400	159	[38]
Ni–S alloy matrix doping CeO_2	Basic	400	165	[39]

Table S15. Comparison of Raman parameters for CeO_{2-x}, Mo-CeO_{2-x}, and Ru-CeO_{2-x}

Parameter	Oxidation			Reduction		
	CeO_{2-x}	Mo-CeO_{2-x}	Ru-CeO_{2-x}	CeO_{2-x}	Mo-CeO_{2-x}	Ru-CeO_{2-x}
F_{2g} peak shift (cm^{-1})	462	458	449	463	460	451
$I_{600+1158}/I_{F2g}$ (Defects)	0.036	0.031	0.168	0.052	0.090	0.203

Reference:

[1] Y. Dou, T. Liao, Z. Ma, D. Tian, Q. Liu, F. Xiao, Z. Sun, J. H. Kim, S. X. Dou, *Nano Energy,* **2016**, 30, 267-275.

[2] Y. Lu, J. Wang, S. Zeng, L. Zhou, W. Xu, D. Zheng, J. Liu, Y. Zeng, X. Lu, *J. Mater. Chem. A*, **2019**, 7, 21678.

[3] Y. Chao, P. Zhou, N. Li, J. Lai, Y. Yang, Y. Zhang, Y. Tang, W. Yang, Y. Du, D. Su, Y. Tan, *Adv. Mater.,* **2019**, 31, 1807226.

[4] Q. Shi, T. Liu, Q. Li, Y. Xin, X. Lu, W. Tang, Z. Zhang, P.X. Gao, J. A. Anderson, *Appl. Catal. B*, **2019**, 246, 312-321.

[5] X. Jin, Y. Duan, D. Liu, X. Feng, W. Li, Z. Zhang, Y. Zhang, *ACS Appl. Nano Mater.,* **2019**, 2, 5769-78.

[6] W. Li, D. Liu, X. Feng, Z. Zhang, X. Jin, Y. Zhang, *Advanced Energy Materials*, **2019**, 9, 1803583.

[7] J. Ran, J. Qu, H. Zhang, T. Wen, H. Wang, S. Chen, L. Song, X. Zhang, L. Jing, R. J. Zheng,S.Z. Qiao, *Adv. Energy Mater.,* **2019**, 9, 1803402.

[8] L. Peng, P. Xiong, L. Ma, Y. Yuan, Y. Zhu, D. Chen, X. Luo, J. Lu, K. Amine, G. Yu, *Nat. Commun.,* **2017**, 8, 1.

[9] Q. Dai, S. Bai, H. Li, W. Liu, X. Wang, G. Lu, *CrystEngComm,* **2014**, 16, 9817.

[10] J. Jia, W. Sun, Q. Zhang, X. Zhang, X. Hu, E. Liu, J. Fan, *Appl. Catal. B,* **2020**, 261, 118249.

[11] W.D. Nesse, *Introduction to mineralogy,* Sidalc, New York,USA, **2012**.

[12] I. Kosacki, T. Suzuki, H. U. Anderson, P. Colomban, *Solid State Ion.*, **2002**, 149, 99.

[13] E. Sartoretti, C. Novara, F. Giorgis, M. Piumetti, S. Bensaid, N. Russo, D. Fino, *Sci. Rep.*, **2019**, 9, 1.

[14] M. Dieterle, G. Mestl, *Phys. Chem. Chem. Phys.*, **2002**, 4, 822.

[15] D. Van Pham, R. A. Patil, J.-H. Lin, C.-C. Lai, Y. Liou, Y.R. Ma, *Nanoscale*, **2016**, 8, 5559.

[16] E. Haro-Poniatowski, C. Julien, B. Pecquenard, J. Livage, M.A. Camacho-López, *J. Mater. Res. Technol*, **1998**, 13, 1033.

[17] Y. Wu, G. Hu, Y. Xie, M. Guo, M. Luo, *Solid State Sci.*, **2011**, 13, 2096.

[18] X. Du, L. Dong, C. Li, Y. Liang, Y. Chen, *Langmuir*, **1999**, 15, 1693.

[19] S. Mar, C. Chen, Y. Huang, K.K. Tiong, *Appl. Surf. Sci.*, **1995**, 90, 497.

[20] H.C. Jo, K.M. Kim, H. Cheong, S.H. Lee, S.K. Deb, *Electrochemical and Solid State Letters*, **2005**, 8, E39.

[21] L. Brewer, R.H. Lamoreaux, *Bulletin of Alloy Phase Diagrams*, **1980**, 1, 85.

[22] L. Wang, Y. Yu, H. He, Y. Zhang, X. Qin, B. Wang, *Sci. Rep.*, **2017**, 7, 1.

[23] R.M. Rakhmatullin, V.V. Semashko, S.L. Korableva, A.G. Kiiamov, A.A. Rodionov, R. Tschaggelar, J.A. van Bokhoven, C. Paun, *Mater. Chem. Phys.*, **2018**, 219, 251.

[24] D. Srinivas, C. Satyanarayana, H. Potdar, P. Ratnasamy, *Appl. Catal., A*, **2003**, 246, 323.

[25] J. Soria, J. Conesa, A. Martınez-Arias, *Colloids and Surfaces A: Physicochemical and Engineering Aspects*, **1999**, 158, 67.

[26] M. Skaf, S. Hany, S. Aouad, C. Gennequin, M. Labaki, E. Abi-Aad, A. Aboukaïs, *Phys. Chem. Chem. Phys.*, **2016**, 18, 29381.

[27] A. Martínez-Arias, J.C. Conesa, J. Soria, *Research on Chemical Intermediates*, **2007**, 33, 775.

[28] A. Martínez-Arias, M. Fernández-García, C. Belver, J.C. Conesa, J. Soria, *Catal. letters*, **2000**, 65, 197.

[29] J.M. Coronado, A.J. Maira, A. Martínez-Arias, J.C. Conesa, J. Soria, *Photochemistry and Photobiology A: Chemistry*, **2002**, 150, 213.

[30] R.M. Rakhmatullin, V.V. Pavlov, V.V. Semashko, *physica status solidi (b)*, **2016**, 253, 499.

[31] Y. Lee, G. He, A. J. Akey, R. Si, M. Flytzani-Stephanopoulos, I.P. Herman*, J. Am. Chem. Soc.*, **2011**, 133, 12952.

[32] E. Abi-Aad, A. Bennani, J.P. Bonnelle, A. Aboukaïs, *J. Chem. Soc.,* **1995**, 91, 99.

[33] W. Wang, Q. Zhu, Q. Dai, X. Wang, *Chem. Eng. Technol.*, **2017**, 307, 1037.

[34] S. Aškrabić, Z. Dohčević-Mitrović, V.D. Araújo, G. Ionita, M.M. de Lima Jr, A. Cantarero, *J. Phys. D Appl. Phys.*, **2013**, 46, 495306.

[35] K.S. Hemalatha, K. Rukmani, *RSC advances*, **2016**, 6, 74354.

[36] Z. Zheng, N. Li, C.Q. Wang, D.Y. Li, Y.M. Zhu, G. Wu, *Int. J. Hydrog. Energy*, **2012**, 37, 13921.

[37] S.S. Zhang, *Frontiers in Energy Research*, **2013**, 1, 10.

[38] X. Long, H. Lin, D. Zhou, Y. An, S. Yang, *ACS Energy Letters*, **2018**, 3, 290.

[39] M. Zhao, H. Dong, Z. Chen, Z. Ma, L. Wang, G. Wang, W. Yang, G. Shao, *Int. J. Hydrog. Energy*, **2016**, 41, 20485.